Conducted Common-Mode EMI Modeling of Active Magnetic Bearings Based on Multiaxis Online Impedance Measurement

Yuanhao Xie, *Graduate Student Member, IEEE*, Dong Jiang, *Senior Member, IEEE*, Hui Liu, *Graduate Student Member, IEEE*, and Zicheng Liu, *Senior Member, IEEE*

***Abstract*—The active magnetic bearing (AMB) driven by power electronic converters is an emerging technique in the industry to suspend high-speed rotating machinery. The high-frequency switching of the converter can bring electromagnetic interference (EMI) to the system, affecting its reliable operation. This article focuses on the modeling of common mode (CM) EMI in multiaxis AMB systems. The impedance characteristics should be measured online due to the variation of rotor position. Thus, the multiaxis online impedance measurement scheme has been proposed in this article. The impedance measurement requires consideration of both signal-to-noise ratio and independence of different excitation tests. The CM equivalent circuit model has also been built and the parameters have been extracted with a two-step fitting scheme. The experiment has been done to prove the effectiveness of the proposed model. With the proposed method, the CM EMI of multiaxis AMB can be precisely predicted. Furthermore, the CM EMI filter has been designed for the AMB based on the proposed model.**

***Index Terms*—Active magnetic bearing (AMB), electromagnetic interference (EMI), online impedance measurement.**

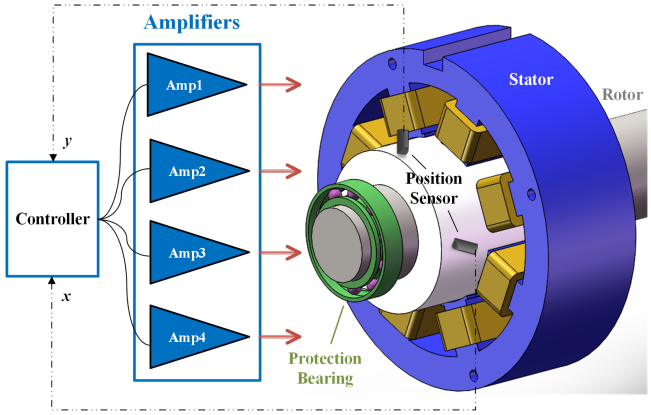

Fig. 1. Typical 8-pole 2-DOF radial AMB system.

I. Introduction

THE active magnetic bearing (AMB) is an advanced bearing system that utilizes the controllable electromagnetic force to suspend the shaft. Unlike the traditional mechanical bearings, the rotor is suspended in the air so that there's nearly zero friction and no more need for lubricant. These unique characteristics make AMB a better choice for high-speed rotating machinery [1]. Furthermore, the controllable electromagnetic force provides more degrees of freedom (DOF) for the rotating system to optimize the performance. Nowadays, AMBs are increasingly widely used in industry scenarios including flywheel, turbomachinery, etc.

The typically used eight-pole 2-DOF radial AMB is shown in Fig. 1. For each DOF, two magnets are used together to generate forces in opposite directions. The rotor has 6-DOFs in total, and all 5-DOFs except for axial rotation need to be controlled by the AMBs. As a result, a complete AMB system should include two of the aforementioned radial AMBs and one thrust AMB [2].

The reliability of the AMB controller is of vital importance to high-speed machinery applications. The power electronic converter is widely used as the power amplifier to drive each winding of the AMBs. The high-frequency (HF) switching actions of the converter will continuously emit electromagnetic interference (EMI) to the system, which becomes a significant threat to the reliability of the surrounding equipment as well as AMB itself. On one hand, the emitted EMI will affect the external power supply equipment and, therefore, should comply with industrial EMI standards. On the other hand, the common mode (CM) EMI caused by the converter is found easily coupled to the displacement sensor so that it deteriorates the performance of suspension [3]. Therefore, the EMI of AMB system, especially CM EMI, should be suppressed. Kagalwala and Shenoy [4] and Andrade et al. [5] have mentioned EMI filters for AMB drive systems, but due to the lack of HF model, the design procedure can be empirical and time consuming, and may lead to a large volume of EMI filters. As a result, the analysis and understanding of the CM EMI characteristics of the AMB are essential for designing suppression strategies, but they are seldom mentioned in previous research works.

Received 6 April 2024; revised 27 August 2024; accepted 2 October 2024. Date of publication 8 October 2024; date of current version 12 December 2024. This work was supported in part by the National Natural Science Foundation of China (NSFC) under Grant 52477189. Recommended for publication by Associate Editor M. Tavakoli Bina. *(Corresponding author: Dong Jiang.)*

The authors are with the State Key Laboratory of Advanced Electromagnetic Engineering and Technology, School of Electrical and Electronic Engineering, Huazhong University of Science and Technology, Wuhan 430074, China (e-mail: xieyh@hust.edu.cn; jiangd@hust.edu.cn; liuhuihui@hust.edu.cn; liuzc@hust.edu.cn).

Color versions of one or more figures in this article are available at https://doi.org/10.1109/TPEL.2024.3476343.

Digital Object Identifier 10.1109/TPEL.2024.3476343

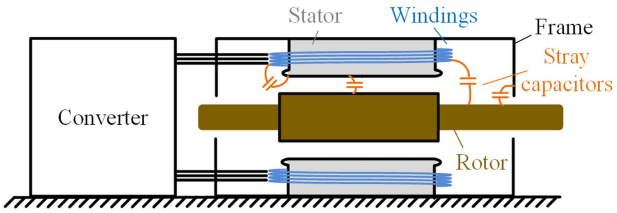

Fig. 2. Parasitic capacitors inside the AMB.

Considering a single radial AMB, Fig. 2 shows its inner structure and the parasitic capacitors. There are three parts of conductors: stator/frame, windings, and rotor. They are coupled together through the stray capacitors to form the flow path of the CM leakage current. Therefore, its HF CM characteristics are pretty much like an ac motor in [6].

Literature works have well documented the HF model of the ac motors. Magdun and Binder [7] and Wu et al. [8] have presented several types of lumped parameter models of the motor, using the ideal *R-L-C* elements to present the characteristics of windings, frame, and even parasitic parameters. Another kind of HF modeling method is called "behavior modeling," where only the terminal impedance behavior is considered, and the structure and the characteristics analysis of the motor components are not needed [9]. Both the two modeling methods have shown good accuracy in predicting the EMI of the motor drive system. However, different from the ac motor, the 5-DOF AMB system has multiple HF interference sources that are coupled together through the suspended rotor to generate the total conducted EMI [3]. As a result, the HF behavior of the multi-DOF AMB system is much more complicated than that of ac motors.

The HF characteristics of the AMB system should be measured before building the model. For the ac motors, the port impedances can be measured offline by an impedance analyzer or vector network analyzer (VNA) [10], because the influence of the mechanical load and speed of the motor on its CM impedance in the medium- to high-frequency range is negligible [11]. However, with respect to the AMB system, the rotor position can be changed by the active control. More importantly, the air gap between the frame and the rotor will only exist when the control system is working online and the rotor is suspended. As a result, the online impedance measurement becomes a must for the HF modeling of the AMB system.

Several online impedance measurement methods have been well-established for power electronics systems [12]. The existing online measurement methods can be divided into two categories, the V-I approach [13] and the VNA-based approach [14], [15]. These methods have been proven to have a good signal-to-noise ratio (SNR) when implemented in motor drive systems. The VNA-based approach identifies system network parameters by injecting HF signals into the system and measuring the responses, then the impedance can be calculated from network equations [16]. For the AMB system, multiple injection signals are required and multiple responses should be measured simultaneously. To avoid the impact of inherent system noise caused by the converter and improve the SNR, the injection amplification and measurement attenuation are needed. Therefore, a large number of RF devices are needed to complete the impedance identification of the multi-DOF AMB system. On the contrary, the V-I approach utilizes the inherent HF voltage excitation and current response to achieve impedance testing, which is much easier to implement to the AMB system. Still, all these methods considered the tested target as a single input single output system so that the impedance can be easily identified, but new challenges arise when measuring the AMB system with multiple mutually coupled interference sources.

TABLE I
LISTS OF LITERATURE REVIEWS

	Literatures	Limitations	This Paper's Work
Impedance Measurement Methods	Offline measurement [7] [8] [10]	Can not handle that the impedance of AMB changes with rotor position.	V-I based online HF impedance identification with multiple EMI sources
	VNA based online method [14] [15] [16]	Only for single CM source, needs lots of RF devices.	
	V-I based online method [13]	Only for single CM source.	
HF Modeling Methods	Previous work [3]	Only pre analysis, showing that AMB system has coupled multiple CM EMI sources.	Lumped-parameter modeling and prediction of EMI in AMB system
	Lumped parameter model [7] [8]	Only for AC motors, lack of CM EMI analysis of AMB.	
	Behavior model [9]		

All the above-mentioned literatures are listed in Table I along with their limitations. This article aims to quantitatively analyze the CM EMI problem and build the HF CM model of the multiaxis AMB system, which is essential for the design of EMI filters or other EMI suppression strategies. To the extent of the authors' knowledge, all the existing methods are not capable of identifying the complex CM characteristics of the multi-DOF AMB. The major contribution of this article is to extend the online identification method of HF impedance to complex systems with multiple interference sources coupled together. Minor contributions include analyzing the CM impedance characteristics of the 5-DOF AMB, proposing a lumped parameter equivalent model for it, and providing a two-step fitting method to determine a large number of parameters, thus finally achieving the target of predicting the CM EMI of the AMB system. And the model is further implemented to effectively design the EMI filter for the AMB drive system.

The rest of the article is organized as follows. The structure of the AMB system and its CM characteristics are analyzed in Section II. The multiaxis online measurement method is proposed in Section III. The lumped parameter CM model of the AMB system is built in Section IV. The experiments are carried out in Section V to verify the proposed model. An EMI filter prototype is designed for AMB in Section VI.

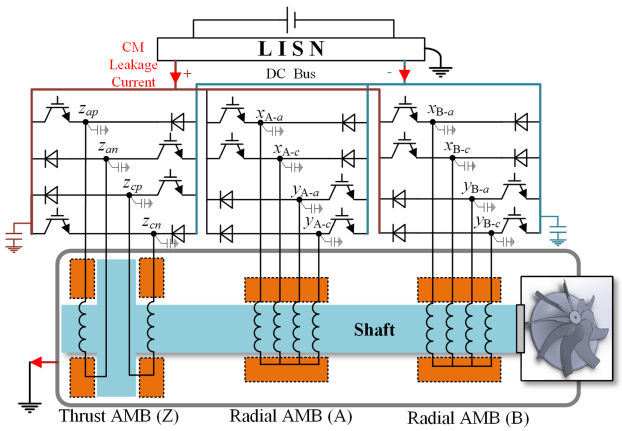

Fig. 3. System structure of the 5-DOF AMB and the converter.

TABLE II
SPECIFICATIONS OF THE AMB EXPERIMENT PLATFORM

Parameters	Values
Rotor mass	4.5 kg
Switching frequency	20 kHz
Rated DC bus voltage	150 V
Protection bearing air gap	250 μm
Designed winding inductance	0.4 mH (radial AMBs) 2m H (thrust AMB)
Bias winding current	2.4 A
Maximum winding current	4.8 A

II. CM CHARACTERISTICS OF THE AMB SYSTEM

The system structure of the 5-DOF AMB and its power electronic converter are shown in Fig. 3, with the specifications presented in Table II. Note that all the experiments and simulations in this article are based on AMB platform. The AMB system consists of two radial AMBs and one thrust AMB, which are named AMB-A, AMB-B, and AMB-Z in this article. To control the electromagnetic force in the 5-DOF AMB, two four-leg converters are implemented to drive the radial AMB and two half H-bridges are used to drive the thrust AMB [3]. Such configurations are profitable for the online impedance measurement, which will be introduced in the next section. The HF switching of the converter will generate leakage current through the stray capacitors between the switching devices and the heat sink, and also those between the AMB windings and the frame. The line impedance stabilization network (LISN) is added at the dc inputs of the AMB converter for the EMI test.

In order to analyze the CM EMI problem, the first thing is to define the CM voltages (CMV) of the AMB system. Thus, the VNA-based offline measurements are carried out to understand its basic characteristics. The AMB system has a total of 12 input ports, with 4 ports for each AMB part. All the windings are left floated without any connections and the impedances between the ports and the frame are measured with VNA, the results are shown in Fig. 4. It can be seen that for each specific AMB part, the impedance of each port to the frame is almost identical, thanks to the symmetrical arrangement of the windings. Therefore, we can define three CMV sources corresponding to three

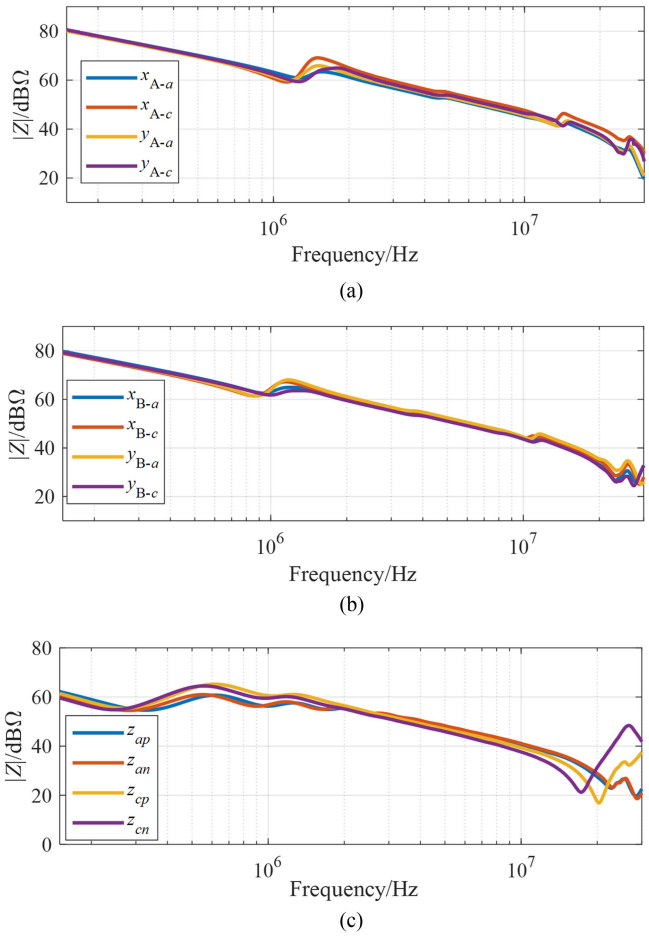

Fig. 4. Offline measured impedance between ports to frame. (a) AMB-A. (b) AMB-B. (c) AMB-Z.

AMB parts. Each CMV can be expressed as

$$V_{\mathrm{CM}} = \frac{1}{4}\sum_{i=1}^{4} V_i \tag{1}$$

where V_i is the voltage added to the port of AMB. The small deviations between the four ports within one specific AMB part are mainly due to the rotor not being at the geometric center during offline measurements. The rotor position will significantly influence the air gap, thus deciding the winding inductance, and further affecting the resonance frequency and amplitude of winding inductance and stray capacitance. That is why the biggest impedance deviations shown in Fig. 4 happen at the first two resonance peaks. This can also support the necessity of online measurement.

Next, taking one port of each AMB part out to laterally compare their impedance to the frame, the results are shown in Fig. 5. It can be seen from Fig. 5 that different AMB parts have significantly different CM impedance characteristics. Thus, the defined three CMV cannot be combined into one.

Therefore, the 5-DOF AMB should be modeled as a multi-input-single-output system as shown in Fig. 6. The converter will generate three CMVs and form leakage current $I_{\mathrm{CM\text{-}C}}$ through the stray capacitance C_p and $C_{p\text{-}\mathrm{dc}}$. The source impedances are mainly decided by the inductance of PCB trace which are far

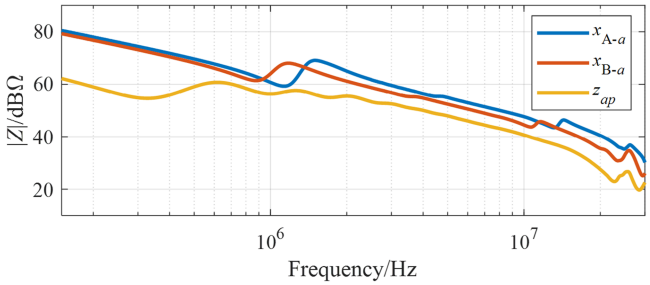

Fig. 5. Lateral comparison of impedance of port 1 of three AMB parts.

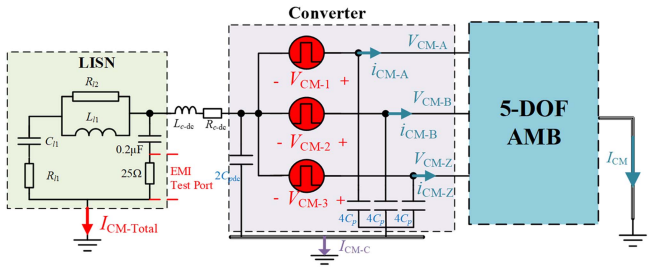

Fig. 6. Overall equivalent model of the 5-DOF AMB system.

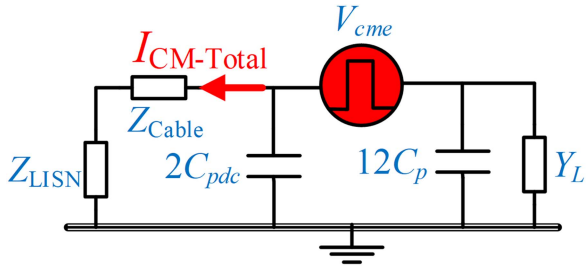

Fig. 7. Simplified equivalent circuit of the AMB system.

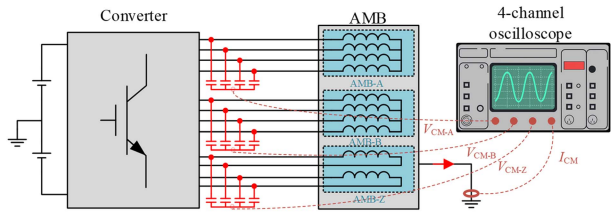

Fig. 8. Online measurement configurations.

smaller than that of AMB windings and power cables and have little influence on the EMI prediction, thus they can be omitted.

For the AMB, the input CMVs of its three bearing parts are noted as $V_{\text{CM-}A}$, $V_{\text{CM-}B}$, and $V_{\text{CM-}Z}$. These three input CM sources are coupled through the complex impedance network inside the AMB and ultimately generate a CM current through the grounding wire of the frame. Based on Ohm's law, the CM equivalent circuits of the 5-DOF AMB can be presented as

$$\boldsymbol{I} = \boldsymbol{Y}\boldsymbol{U} \tag{2}$$

where

$$\boldsymbol{I} = \begin{bmatrix} i_{\text{CM}-A} \\ i_{\text{CM}-B} \\ i_{\text{CM}-Z} \end{bmatrix}, \quad \boldsymbol{Y} = \begin{bmatrix} Y_{AA} & Y_{BA} & Y_{ZA} \\ Y_{AB} & Y_{BB} & Y_{ZB} \\ Y_{AZ} & Y_{BZ} & Y_{ZZ} \end{bmatrix},$$

$$\boldsymbol{U} = \begin{bmatrix} V_{\text{CM}-A} \\ V_{\text{CM}-B} \\ V_{\text{CM}-Z} \end{bmatrix}.$$

It is noted that all the variables are in the frequency domain and the symbol $j\omega$ is omitted. Then, I_{CM} can be calculated as

$$I_{\text{CM}} = i_{\text{CM}-\text{A}} + i_{\text{CM}-\text{B}} + i_{\text{CM}-\text{Z}} = Y_A V_{\text{CM}-\text{A}} + Y_B V_{\text{CM}-\text{B}} + Y_Z V_{\text{CM}-\text{Z}} \tag{3}$$

where

$$Y_A = Y_{AA} + Y_{AB} + Y_{AZ}, Y_B = Y_{BA} + Y_{BB} + Y_{BZ}, Y_Z = Y_{ZA} + Y_{ZB} + Y_{ZZ}.$$

Then, the AMB system can be simplified using Thevenin's equivalence as shown in Fig. 7, where the equivalent CMV V_{cme} and equivalent load admittance Y_L can be presented as

$$V_{cme} = \frac{V_{\text{CM}-1}Y_A + V_{\text{CM}-2}Y_B + V_{\text{CM}-3}Y_Z + 4C_p\sum_{i=1}^{3} V_{\text{CM}-i}}{Y_A + Y_B + Y_Z + 12C_p} \tag{4}$$

$$Y_L = Y_A + Y_B + Y_Z. \tag{5}$$

III. Multiaxis Online Impedance Identification Method

As mentioned in Part II, the online impedance measurement is essential for the HF modeling of the AMB. According to (4) and (5), only three parameters Y_A, Y_B, and Y_Z, should be identified to achieve the EMI prediction. Other parameters in Fig. 7 can be measured independently with an impedance analyzer. Also, the V-I approach is selected as the basic measurement principle of this article which is easier to implement compared with VNA-based online measurement method.

A. V-I Measurement Principle of the AMB

The basic principle of V-I measurement is Ohm's law, as has been presented by (3). The input CMVs of AMB's three bearing parts, $V_{\text{CM-A}}$, $V_{\text{CM-B}}$, and $V_{\text{CM-Z}}$, can be obtained using star-connected parallel capacitors and measured by high-voltage differential probes. The CM current in the grounding cable of the AMB frame is measured with the current probe. The CMVs and current are measured simultaneously using the 4-channel oscilloscope and transformed into the frequency domain. The measurement configurations are shown in Fig. 8.

To identify the three admittance parameters, at least three independent measurements are needed. The measurement results can be presented as

$$\boldsymbol{I}_{\text{meas}} = \boldsymbol{U}_{\text{meas}}\boldsymbol{Y}_1 \tag{6}$$

where

$$\boldsymbol{I}_{\text{meas}} = \begin{bmatrix} i_{\text{CM}-1} \\ i_{\text{CM}-2} \\ i_{\text{CM}-3} \end{bmatrix}, \quad \boldsymbol{U}_{\text{meas}} = \begin{bmatrix} V_{\text{CM}-\text{A1}} & V_{\text{CM}-\text{B1}} & V_{\text{CM}-\text{Z1}} \\ V_{\text{CM}-\text{A2}} & V_{\text{CM}-\text{B2}} & V_{\text{CM}-\text{Z2}} \\ V_{\text{CM}-\text{A3}} & V_{\text{CM}-\text{B3}} & V_{\text{CM}-\text{Z3}} \end{bmatrix},$$

$$\boldsymbol{Y}_1 = \begin{bmatrix} Y_A \\ Y_B \\ Y_Z \end{bmatrix}.$$

The footmarks 1, 2 and 3 are measurement numbers. The $\boldsymbol{Y}_1$ can be calculated by (7) on the condition that $\boldsymbol{U}_{\text{meas}}$ is nonsingular

$$\boldsymbol{Y}_1 = \boldsymbol{U}_{\text{meas}}{}^{-1} \boldsymbol{I}_{\text{meas}}. \tag{7}$$

The identification of admittance is now theoretically feasible, but there are still two practical problems. On one hand, since the voltages and currents are measured in a time domain and transformed into the frequency domain, there are inevitable measurement errors and spectral leakage problems, thus the method of signal processing will significantly influence the SNR and precision of the identification results. On the other hand, to ensure the nonsingularity of $\boldsymbol{U}_{\text{meas}}$, the voltage vectors obtained from three measurements must be linearly independent in the whole frequency range. This is not easy to realize especially in high frequency above MHz.

B. Signal Processing to Extract the Impedance

To calculate formula (7), both the phase and amplitude of the currents and voltages within the whole frequency range are needed. Chen et al. [17] have documented an all-phase FFT (apFFT) method with intermediate-frequency filtering, which has shown the capability to suppress the spectrum leakage and obtain the correct impedance phase of the measured motor. The online measurement method presented in both [13] and [17] has proved that the peak points of the spectrums have the minimum error caused by the window function of the FFT algorithm.

A measurement example is taken out here to illustrate the issue. The CMVs of AMB-A are tested in three independent measurements, which are recorded as $V_{\text{CM-}A1}$, $V_{\text{CM-}A2}$, and $V_{\text{CM-}A3}$, and they are transformed into the frequency domain using apFFT, the results are shown in Fig. 9. For power electronic converters, its CM EMI is mainly concentrated in the switching frequency and its integer multiple frequencies. It can be seen in Fig. 9(a) that the first peak point of the spectrum corresponds to the switching frequency which is set as 20 kHz. However, the amplitude of the spectrum between the two peaks is very small, which would be easily influenced by measurement error and result in low SNR, thus, these are invalid frequency points for impedance extraction.

The peak points of the spectrum of $V_{\text{CM-}A1}$ are picked out with the algorithm presented in [17], the frequencies of these points are noted as $\boldsymbol{f}_{\text{p}}(l)$, $l = 12{,}3 \ldots n$, where n is the total number of these peak points. The spectral points of $V_{\text{CM-A2}}$ and $V_{\text{CM-A3}}$ correspond to $\boldsymbol{f}_{\text{p}}(l)$ and are shown in Fig. 9(b) and (c) with red asterisks. It can be seen that these frequency points are far from the envelope of the spectrum especially in frequencies above 1 MHz. The worst case has been marked by

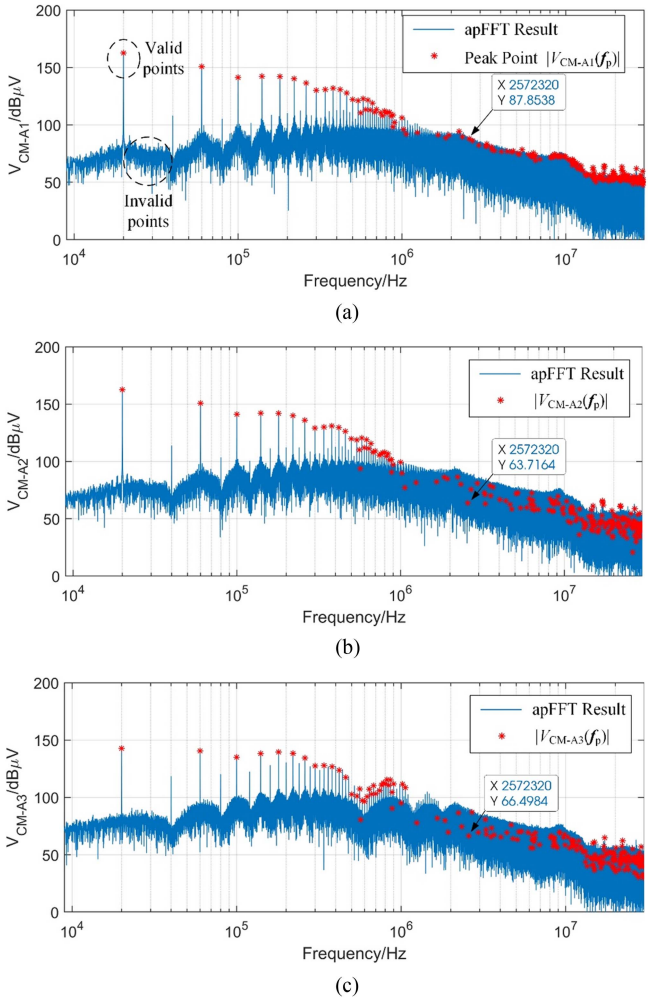

Fig. 9. Spectrum and the peak points of the CMVs of AMB-A. (a) $V_{\text{CM-A1}}$. (b) $V_{\text{CM-A2}}$. (c) $V_{\text{CM-A3}}$.

data tip at 25 72 320 Hz, which is nearly 20 dB smaller than its corresponding envelop lines. Therefore, these frequency points are no longer valid when considering multiple measurements.

To cope with this problem, a multispectral envelope algorithm is proposed to identify a series of points k_{valid} among all frequency points such that the spectral magnitudes of all 12 variables are near their respective envelope lines at these selected points. The process of the algorithm is shown in Fig. 10. The measured 12 voltages and currents ($V_{\text{CM-A1}}$, $V_{\text{CM-A2}}$, …, $V_{\text{CM-Z3}}$, $i_{\text{CM-1}}$, $i_{\text{CM-2}}$, $i_{\text{CM-3}}$) are transformed to the frequency domain with apFFT, so that we can get 12 spectrums as the input of the algorithm, noted as $U_m(k)$, $m = 1 \ldots 12$, $k = 1 \ldots N$, where N is the number of sampling points.

First, the peak points of each spectrum are picked out, noted as $U_m(k_{\text{peak}})$, where k_{peak} is the index of the peak points. For each point of $U_m(k)$, define the adjacent points vector as

$$\boldsymbol{W}_m(k) = [U_m(k-5), \cdots, U_m(k-1), U_m(k+1), \ldots, U_m(k+5)]. \tag{8}$$

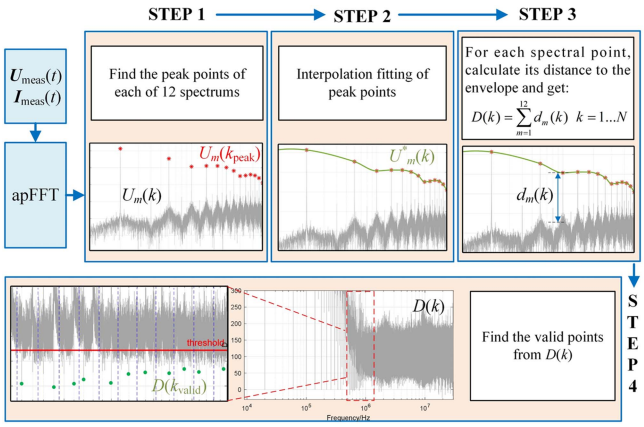

Fig. 10. Multispectral envelop algorithm.

The criterion for determining the peak points are

$$\begin{cases} U_m(k) > \max(\boldsymbol{W}_m(k)) \\ \mathrm{var}([\boldsymbol{W}_m(k),\ U_m(k)]) > p_{\mathrm{var}} \\ U_m(k) - \mathrm{mean}(\boldsymbol{W}_m(k)) > p_{\mathrm{mean}} \end{cases} \tag{9}$$

where var is the function to calculate the variance, the mean is the function to calculate the average value, p_{var} and p_{mean} are the threshold for variance and mean. Second, interpolate the peak points of each U_m with a third-order interpolation method to obtain the envelope curves, noted as $U^*{}_m(k)$. Next, calculate the distance from each spectral point to its corresponding envelope and sum them up to get $D(k)$

$$d_m(k) = U^*_m(k) - U_m(k) \tag{10}$$

$$D(k) = \sum_{m=1}^{12} d_m(k). \tag{11}$$

Then, the index of the valid points is picked out from $D(k)$. The whole frequency range is divided into segments. One certain segment can be presented as $\{k' \mid k_s<k'<\mathrm{ceil}(1.01\ k_s)\}$, where k_s is the start index of the segment. For each segment, find the valid index k_{valid} with decision conditions

$$D(k_{\mathrm{valid}}) < p_D \ \ \&\& \ \ D(k_{\mathrm{valid}}) = \min[D(k')] \tag{12}$$

where p_{D} is the threshold. The $U_m(k_{\mathrm{valid}})$ is the result of the multispectral envelop algorithm.

There are three threshold parameters in the algorithm, p_{var}, p_{mean}, and p_{D}. The selection of p_{var} and p_{mean} is basically empiricism, and the method is shown in Fig. 11. First, using the first peak of the spectrum to calculate the initial value p_{var0} and p_{mean0}. When they are set too high, the peak points obtained cannot achieve the envelope of the spectrum; and when they are set too low, a large number of peak points with magnitudes lower than the envelope are also selected, which will deteriorate the SNR ratio of impedance identification. Simultaneously increase or decrease p_{var} and p_{mean} based on the characteristics of the obtained envelope, thus to get the appropriate values, which are set as 35 and 15 dBμV/ dBμA in this article, respectively.

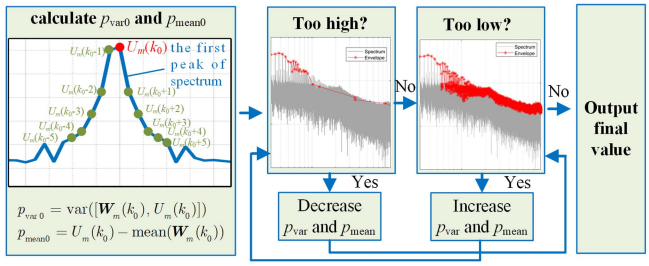

Fig. 11. Selection of p_{var} and p_{mean}.

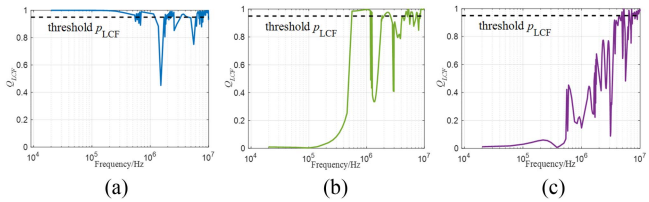

Fig. 12. LCFs of different measurement schemes (a) only change the DC voltage (b) using ZCMPWM and (c) using compensated ZCMPWM (C-ZCMPWM).

As for p_{D}, we have reserved 6 dB margin for each of the 12 variables to avoid selecting spectral points that are more than 50% smaller than their envelopes. Thus $p_{\mathrm{D}} = 6{\times}12 = 72$ dB.

C. Method to Create the Linearly Independent Measurements

Next, these valid frequency points should undergo the linear correlation check before implemented to calculate (7). As mentioned before, the voltage vectors obtained from three measurements should be linearly independent in the whole frequency range. Actually, due to the inevitable measurement errors, they cannot be strictly linearly correlated, but a certain degree of linear correlation still affects the effectiveness of the measurement results. Therefore, the degree of linear correlation needs to be quantitatively described. For any two measured voltage vectors, their linear correlation factor (LCF) can be defined as the cosine of the angle

$$Q_{ab}(j\omega) = \frac{\boldsymbol{U}_a(j\omega)\cdot\boldsymbol{U}_b(j\omega)}{|\boldsymbol{U}_a(j\omega)|\times|\boldsymbol{U}_b(j\omega)|} \quad a,b=1,2,3. \tag{13}$$

And the final LCF can be defined as

$$Q_{\mathrm{LCF}}(j\omega) = \max[Q_{ab}(j\omega)]. \tag{14}$$

To get smaller Q_{LCF}, the spectral characteristics of the CMVs should be reshaped in different individual measurements. Since the measurement should be implemented on the condition that the rotor is suspended, the performance of the position control should not be affected, which means that only the modulation strategy and the dc voltage of the power electronic controller can be modified to fulfill the requirement.

In case that only the dc bus voltages are changed in the three individual measurements, the Q_{LCF} is plotted in Fig. 12(a). Actually, each CMV is multiplied by the same coefficient when the dc voltage changes, so that the LCF is high. By selecting a

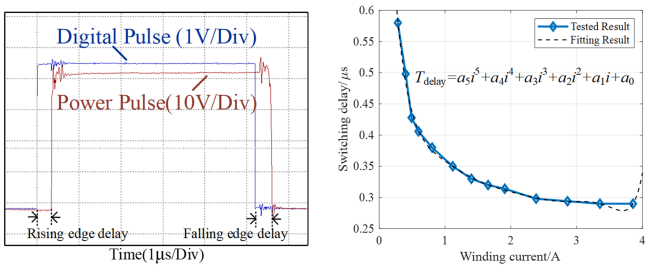

Fig. 13. Switching delay between digital pulse and power pulse. (a) Waveforms. (b) Tested time delay.

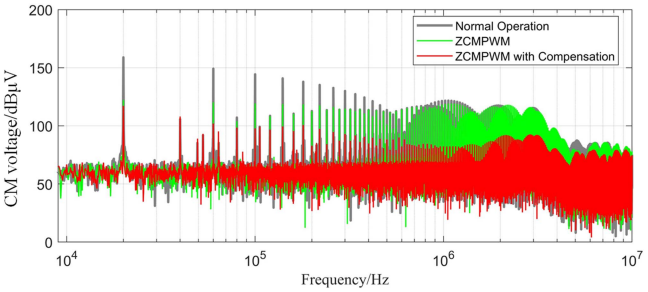

Fig. 14. CMV spectrum comparison between different modulation schemes.

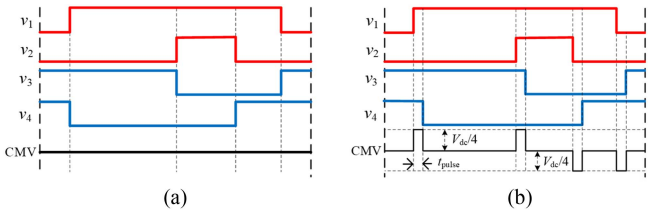

Fig. 15. Four-leg voltages of the converter with (a) ZCMPWM and (b) Q-ZCMPWM.

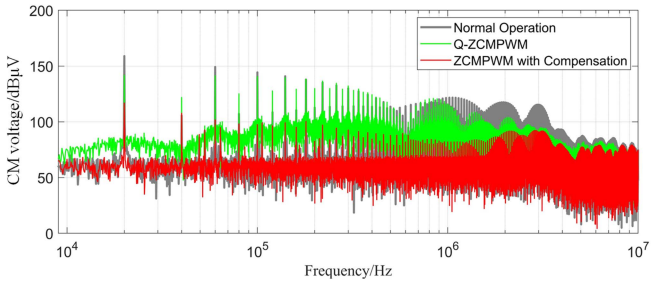

Fig. 16. Spectrum comparison between C-ZCMPWM and Q-ZCMPWM.

threshold $p_{\mathrm{LCF}} = 0.95$ to screen out the data with high LCF, only very few frequency points remain, which are not enough to depict the impedance characteristics.

In our previous work [3], the zero-CM PWM (ZCMPWM) strategy has been proposed to suppress the CM EMI. This modulation strategy can significantly change the HF characteristics of CMV without deteriorating the position control performance, which exactly matches the measurement requirements. It should be noted that the system structure shown in Fig. 3 is needed to implement the ZCMPWM. In three individual measurements, $V_{\mathrm{CM\text{-}A1}}$, $V_{\mathrm{CM\text{-}B2}}$, and $V_{\mathrm{CM\text{-}Z3}}$ in (6) are reshaped using ZCMPWM, and the Q_{LCF} is plotted in Fig. 12(b). It can be seen that the implementation of ZCMPWM effectively reduces the linear correlation, especially in lower frequency bands below 100 kHz. However, the Q_{LCF} is still high in the mid to high-frequency range. The CMVs are tested under normal operation and ZCMPWM, and their spectrums are shown in Fig. 14. It can be seen that the spectral amplitude remains almost unchanged with ZCMPWM in the 1 MHz and higher frequency range. This is due to the inherent limitations of the ZCMPWM, with the most significant being the delay between digital and power pulses.

The tested delay from the digital pulse to the power pulse is shown in Fig. 13(a). The compensation method for switching delay for power electronic converters is well documented in [18], while no literature has done the compensation for the AMB. The controller of the AMB is composed of half bridges with unidirectional currents. Thus, its switching delay is almost only affected by the magnitude of the current. The switching delay of each bridge arm with varied current magnitudes is measured, one of which is shown in Fig. 13(b). The tested curves are fitted with 5th-order polynomial. When the AMB is working, the delay of the rising and falling edges is calculated based on the fitted polynomial using the measured current of each winding, and the delay time is subtracted from the edge of the digital pulse to achieve compensation. The switching delay is compensated based on ZCMPWM, the corresponding spectrum of the CMV is also plotted in Fig. 14. It can be seen that with the compensated ZCMPWM (C-ZCMPWM), the CMV in the mid to high-frequency range is also attenuated. Then, this C-ZCMPWM is implemented to the impedance measurement and the obtained Q_{LCF} is shown in Fig. 12(c). It can be seen that the compensation of switching delay significantly reduces the linear correlation compared to the original ZCMPWM. And with the proposed method, the prerequisite for calculating formula (7) is finally achieved.

D. Further Improvement of SNR

When using the ZCMPWM method for measurement, although the LCF can be reduced, the amplitude of the spectral envelopes of the CMVs are also significantly reduced, resulting in a lower SNR. Therefore, we have made two modifications to the above-mentioned measurement procedure to further improve the SNR.

Firstly, the C-ZCMPWM algorithm is modified as quasi-ZCMPWM (Q-ZCMPWM). The switching waveforms of one four-leg converter within one switching cycle are shown in Fig. 15, where v_1–v_4 are the phase leg voltages and CMV is the CMV. For the Q-ZCMPWM, the phase of v_3 and v_4 are shifted to the right by t_{pulse} compared with C-ZCMPWM. The waveform of the CMV becomes short pulses, the t_{pulse} is set as 2 μs in the experiment. The spectrum of the CMV with Q-ZCMPWM is plotted in Fig. 16. It can be seen that the Q-ZCMPWM does not attenuate the spectrum as much as C-ZCMPWM, which

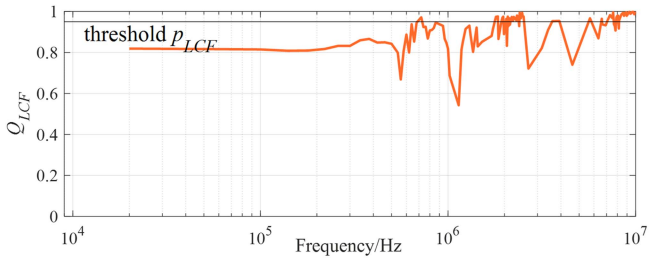

Fig. 17. LCF of the measurement scheme B with Q-ZCMPWM.

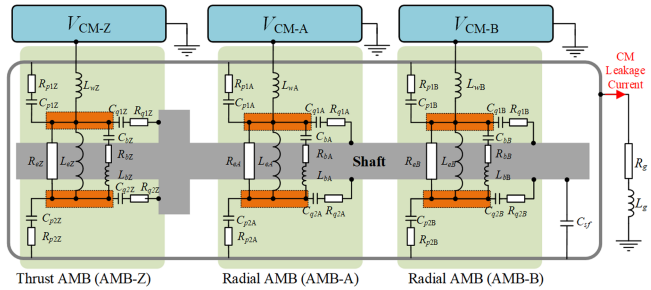

Fig. 18. Lumped parameter equivalent circuits of the 5-DOF AMB.

would result in better SNR. More importantly, the amplitude of frequencies which are even times of switching frequency (20 kHz) are increased, which can be also used as valid frequency points with good SNR.

Second, in the previous measurement arrangement, named scheme A to distinguish from the new one (scheme B), $V_{\text{CM-}A1}$, $V_{\text{CM-}B2}$, $V_{\text{CM-}Z3}$ should be measured with C-ZCMPWM. To improve the SNR, only $V_{\text{CM-}A1}$ and $V_{\text{CM-}B2}$ are measured with Q-ZCMPWM, so that the third individual measurement is in normal operation conditions, resulting in the best SNR.

With the above two modifications, the tested Q_{LCF} is plotted in Fig. 17. Although the linear correlation has increased compared to before, most of the data is still valid. Actually, low linear correlation and high SNR are always two contradictory factors. The improvement of SNR is with the compromise of Q_{LCF}.

IV. Lumped Parameter CM Model of the AMB

The lumped parameter CM equivalent circuit of the 5-DOF AMB system is shown in Fig. 18, where L_w is the inductance of wires, L_e is the winding inductance, R_e is the eddy current loss resistance, C_p and R_p are the parasitic capacitance and resistance between the frame and winding, C_q and R_q are the parasitic capacitance and resistance between the winding and shaft, C_b, R_b, and L_b represent the equivalent impedance of turn-to-turn effect, C_{sf} is the capacitor between the shaft and frame, R_g and L_g are the resistance and inductance of grounding cables. It should be noted that the impedance of AMB-Z is symmetrical. The $C_{p1\text{Z}}$ should be exactly the same as $C_{p2\text{Z}}$, and $C_{q1\text{Z}}$ should be the same as $C_{q2\text{Z}}$, because both ends of each winding are connected to the converter. The value of L_w, R_g, and L_g can be directly measured with VNA.

Next, the parameter values should be extracted from the measured results. The existing extraction methods include analytic calculation [8], automated matching with nonlinear programming or heuristic algorithm [19], finite element analysis [20], etc. Due to the coupling characteristics of multiple CMVs, there are so many parameters in the AMB system. The automated matching with genetic algorithm [19] would be helpful for global optimization, but optimizing a large number of parameters still remains a challenge. Thus, a two-step fitting scheme is proposed to enhance the optimization as well as improve the computational efficiency.

First, fit each bearing part (A, B, or Z) separately. Find parameter vector $\boldsymbol{P}_X$ with the objective presented as

$$\min\ K_{\text{obj}} = \sum_{\omega=2\pi\times 9\text{e}3}^{2\pi\times 1\text{e}7} |G_X(j\omega, \boldsymbol{P}_X) - Y_X(j\omega)|, \quad X = \text{A}, \text{B}, \text{Z} \tag{15}$$

where $G_X(j\omega)$ is the admittance of the lumped parameter circuit for each bearing part. The optimized parameter vector can be noted as $\boldsymbol{P}_1 = \{\boldsymbol{P}_{\text{A}}, \boldsymbol{P}_{\text{B}}, \boldsymbol{P}_{\text{Z}}\}$. For the second step, perform joint optimization on all parameters in a small range, and find the best parameter vector $\boldsymbol{P}_2$

$$\begin{aligned}\min\ K_{\text{obj}} = \sum_{\omega=2\pi\times 9\text{e}3}^{2\pi\times 1\text{e}7} \text{abs}\Big[& G_{\text{A}}^{\text{B,Z}}(j\omega, \boldsymbol{P}_2)\big|_{V_{\text{CM-B}}=0}^{V_{\text{CM-Z}}=0} - Y_{\text{A}}(j\omega) \\ & + G_{\text{B}}^{\text{A,Z}}(j\omega, \boldsymbol{P}_2)\big|_{V_{\text{CM-A}}=0}^{V_{\text{CM-Z}}=0} - Y_{\text{B}}(j\omega) \\ & + G_{\text{Z}}^{\text{A,B}}(j\omega, \boldsymbol{P}_2)\big|_{V_{\text{CM-A}}=0}^{V_{\text{CM-B}}=0} - Y_{\text{Z}}(j\omega)\Big]\end{aligned}$$
$$\text{subject to}\ \ \boldsymbol{P}_2 \in [0.8\boldsymbol{P}_1, 1.2\boldsymbol{P}_1] \tag{16}$$

where $G_{\text{A}}^{\text{B,Z}}$ is the admittance between CM input of AMB-A and ground calculated by equivalent circuit on condition that $V_{\text{CM-B}}$ and $V_{\text{CM-Z}}$ are zero, the same is for $G_{\text{B}}^{\text{A,Z}}$ and $G_{\text{Z}}^{\text{A,B}}$. With the proposed method, we can get the equivalent model of the AMB system. All the measurement and fitting results are presented in Section V.

V. Experimental Validation

The measurements and modeling of the AMB system are based on a 5-DOF AMB compressor platform whose photos are shown in Fig. 19. The switching frequency of the AMB controller is set as 20 kHz, the rated bias current is set as 2.4 A. The oscilloscope used for measurement is ROHDE&SCHWARZ produced RTE1000 with high-resolution mode, where the vertical resolution is 16-bit up to 30 MHz. The dc bus voltage is set as 200 V.

First, the effectiveness of the proposed multispectrum envelop algorithm should be verified. The 12 voltages and currents are measured with the aforementioned scheme B, where $V_{\text{CM-A1}}$ and $V_{\text{CM-B2}}$ are measured with Q-ZCMPWM. The spectrums of the 12 variables are shown in Fig. 20 with blue lines. The yellow lines are the interpolated envelope, and the black asterisks are the valid points after implementing the proposed algorithm. It can be seen that all the valid points are closed to their corresponding spectrum envelopes, this would result in better SNR.

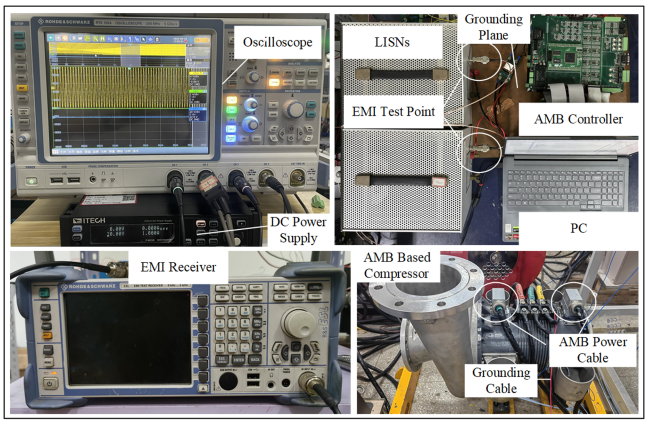

Fig. 19. Experimental platform.

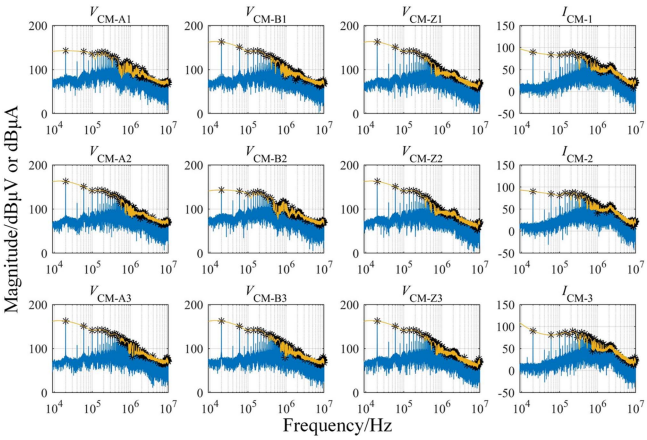

Fig. 20. Results of the multispectral envelop algorithm.

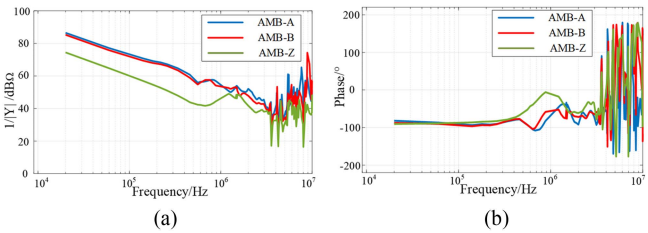

Fig. 21. Impedance measurement results of scheme A. (a) Amplitude. (b) Phase.

Next, the three admittance parameters defined in (3) are extracted from the valid points of the measured 12 variables. The results are shown in Figs. 21 and 22 with both amplitude and phase information. It should be noted that all the admittance is converted to impedance by $Z_x = 1/Y_x$, $x = \mathrm{A}, \mathrm{B}, \mathrm{Z}$.

Fig. 21 shows the extracted impedance measured with scheme A, while Fig. 22 shows those with scheme B. It can be seen that the results from scheme A contain a large amount of noise, especially in the mid to high-frequency range where the SNR is significantly insufficient. However, the results from scheme B show the characteristics of the impedance so clear in the whole frequency range, which indicates that the implementation of the

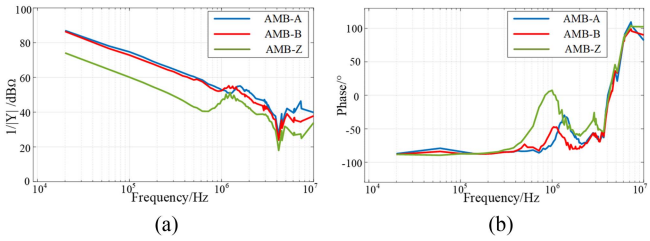

Fig. 22. Impedance measurement results of scheme B. (a) Amplitude. (b) Phase.

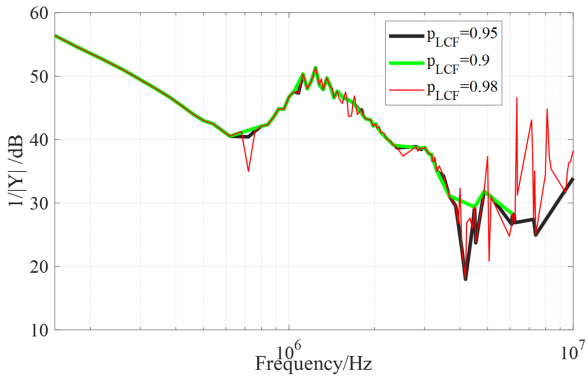

Fig. 23. Impedance measurement results with different LCF threshold.

online measurement of AMB needs to consider both SNR and the linear correlation. The proposed scheme B can significantly improve the SNR at the cost of sacrificing some LCF. Note that the maximum measurement frequency is confined to 10 MHz, which is mainly limited by the sampling accuracy and bandwidth of the oscilloscope and probes. The amplitude of voltage and current signals above 10 MHz is quite small, making them highly susceptible to background noise. In [13], a high-pass filter was implemented to the motor drive system to improve measurement accuracy in the frequency range above 10 MHz, which could be considered for further optimizing the impedance identification results of the AMB.

It can be seen from Fig. 22 that the three CM impedance have a generally consistent trend in the whole frequency range, and the Z_Z is significantly lower than the others, which means that the thrust AMB makes a greater contribution to the CM EMI.

Then, it is also important to verify the impact of the linear correlation between the three individual measurements on the impedance extraction results. To take Z_z as an example, the extracted Z_z with different LCF threshold p_{LCF} is shown in Fig. 23. The 0.95 is what we chose to get the final result shown in Fig. 22. When p_{LCF} is set as 0.98, it can be clearly seen that there are many noise points added to the impedance spectrum. These noise points are caused by the numerical errors while calculating (7) with approximate singular matrix $\boldsymbol{Y}$. On the contrary, when p_{LCF} is set lower as 0.9, the valid frequency points are not enough and some features of the spectrum will be lost. Therefore, the selection of appropriate p_{LCF} should strike a balance between smaller noise and more valid points.

TABLE III
EXTRACTED PARAMETERS OF THE CM MODEL

Parameters	Values	Parameters	Values	Parameters	Values
C_{p1A}	146.3 pF	C_{p2A}	122.4 pF	C_{q1A}	8.0 pF
C_{q2A}	11.2 pF	R_{p1A}	22.6 Ω	R_{p2A}	14.0 Ω
R_{q1A}	147.8 Ω	R_{q2A}	113.9 Ω	L_{eA}	93.0 μH
R_{eA}	1085 Ω	C_{bA}	57.8 pF	L_{bA}	25.7 μH
R_{bA}	101.5 Ω	**Parameters for AMB-A**			
C_{p1B}	188.1 pF	C_{p2B}	120.9 pF	C_{q1B}	15.8 pF
C_{q2B}	12.7 pF	R_{p1B}	4.6 Ω	R_{p2B}	27.2 Ω
R_{q1B}	94.5 Ω	R_{q2B}	116.2 Ω	L_{eB}	173.1 μH
R_{eB}	1748 Ω	C_{bB}	34.9 pF	L_{bB}	38.4 μH
R_{bB}	130.4 Ω	**Parameters for AMB-B**			
C_{p1Z}	315.2 pF	C_{p2Z}	1119 pF	C_{q1Z}	58.4 pF
C_{q2Z}	33.2 pF	R_{p1Z}	1.6 Ω	R_{p2Z}	127.1 Ω
R_{q1Z}	1.6 Ω	R_{q2Z}	2.5 Ω	L_{eZ}	39.0 μH
R_{eZ}	2228 Ω	C_{bZ}	43.4 pF	L_{bZ}	112.5 μH
R_{bZ}	428.8 Ω	**Parameters for AMB-Z**			
R_{l1}	0.1 Ω	C_{l1}	20μF	L_{l1}	2.92 mH
R_{l2}	235 Ω	**Parameters for LISN**			
L_w	1.66 μH	L_g	2.87 μH	R_g	0.075 Ω
$L_{c\text{-}dc}$	0.56 μH	$R_{c\text{-}dc}$	0.057 Ω	C_{sf}	68.5 pF
C_p	16.8 pF	C_{pdc}	95.9 pF	**Others**	

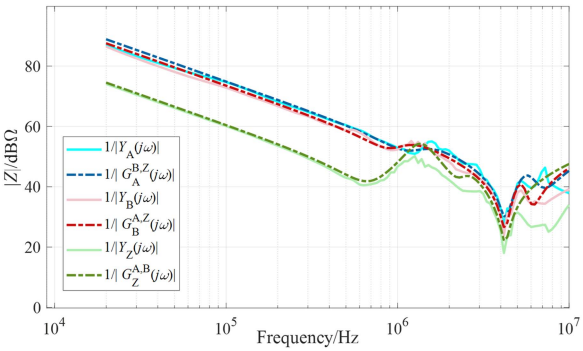

Fig. 24. Fitting results of the impedance.

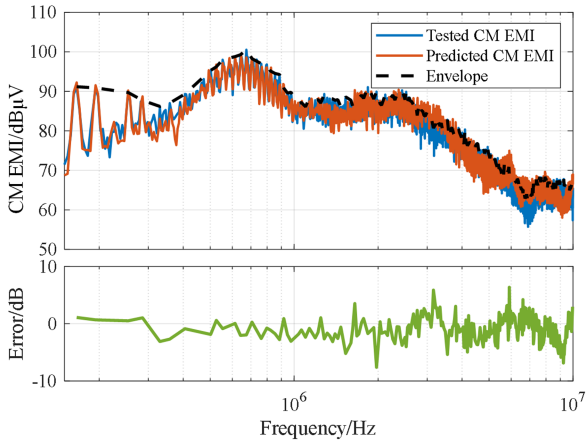

Fig. 25. EMI prediction result.

Using the measured impedance, the parameters of the lumped parameter equivalent circuits of the AMB's CM path can be extracted with the proposed two-step fitting scheme using a genetic algorithm. The fitting results are shown in Fig. 24 with dashed lines and the corresponding 51 parameters are shown in Table III. Also, the impedances of the LISNs, the inductance and resistance of dc power cable, as well as the stray capacitances of the converter are measured offline with VNA. Note that the LISN is fitted with the circuit model in Fig. 6. All these parameters are also shown in Table III. Now we have finally gotten the HF CM model of the 5-DOF AMB system.

To validate the effectiveness of the model, a control experiment is conducted. The dc bus voltage is changed to 150 V, and the switching frequency of the converter is modified to 15 kHz, the AMB works under 5-DOF static suspension condition. The CM EMI is tested using an EMI receiver. Then, the three CMVs as shown in Fig. 6 are measured as excitation and the CMV on the 50 Ω output port of the LISN is simulated based on the HF CM model. The model of an EMI receiver with an intermediate frequency filter and peak detection is established [21]. Finally, the CM EMI can be predicted and compared with the tested results as shown in Fig. 25. The prediction errors of the envelopes are also shown in Fig. 25. The peak of the predicted EMI spectrum is almost consistent with the tested results. The maximum prediction error of the peak of the spectrum is no more than 8 dB. Overall, the predicted results are relatively accurate, proving the effectiveness of the model established in this article.

VI. MODEL-BASED CM EMI FILTER DESIGN FOR AMB

The design of CM EMI filter for the AMB is proposed in this section to further validate the effectiveness of the proposed model as well as to demonstrate a typical application scenario of the model.

First, the CM EMI of the AMB drive system is tested with an EMI receiver on static levitation condition with 150 V dc bus voltage and 20 kHz switching frequency, as shown in Fig. 26(a). The required insertion loss (IL) of the filter is calculated based

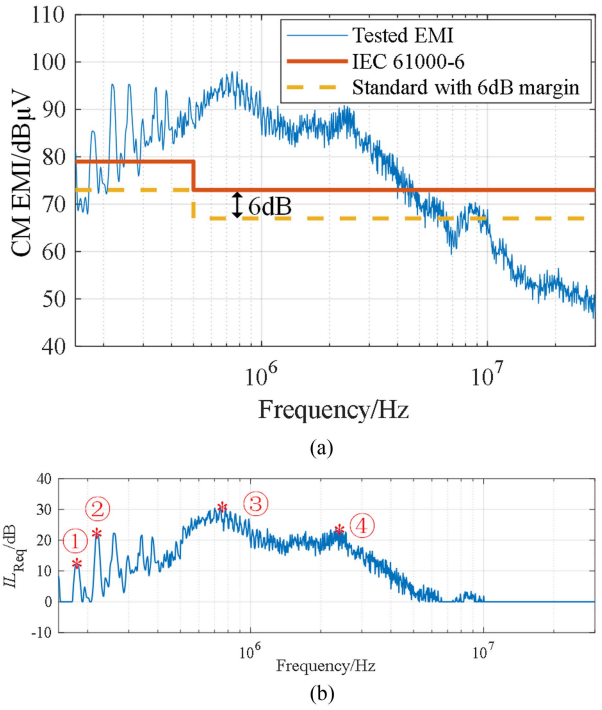

Fig. 26. (a) Measured CM EMI. (b) Required insert loss.

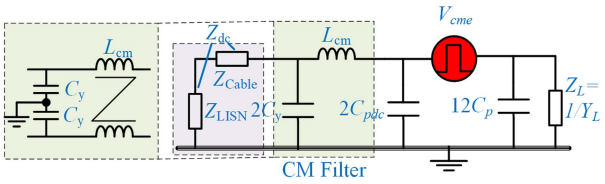

Fig. 27. CM equivalent circuit of the AMB system with EMI filter.

on the industrial standard IEC 61000-6-4 with a reserved 6 dB margin, as shown in Fig. 26(b). The four spectral peak points in Fig. 26(b) are selected as reference values for the IL of the designed filter.

Then, the filter type is selected and the IL should be calculated based on the proposed model. There are several typical CM filter configurations, including *LC*, *CL*, *CLC,* and *LCL* [22]. To avoid resonance, the second-order filters are most commonly used. The *LC* filter would be better to suppress the CMV on the LISN [23], but it will be possible to increase the leakage current of the load side. However, for the AMB, the displacement sensor would be prone to the frame and rotor voltage, thus the leakage current of the AMB should also be suppressed. Therefore, the *CL* filter is selected here in this article.

The equivalent circuit of the AMB drive system along with the *CL* filter is shown in Fig. 27. All the parameters have been defined in Fig. 6 and have been measured or identified with the modeling procedure. The value of the Y capacitor C_y is selected as a typical value 2200 pF, and the insert loss under different $L_{\rm cm}$ is calculated and shown in Fig. 28.

Next, by comparing the four reference points in Fig. 26(b) with the calculated IL in Fig. 28, we can obtain a rough threshold

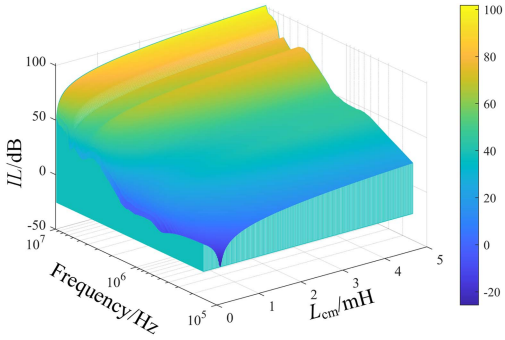

Fig. 28. Predicted IL of the EMI filter.

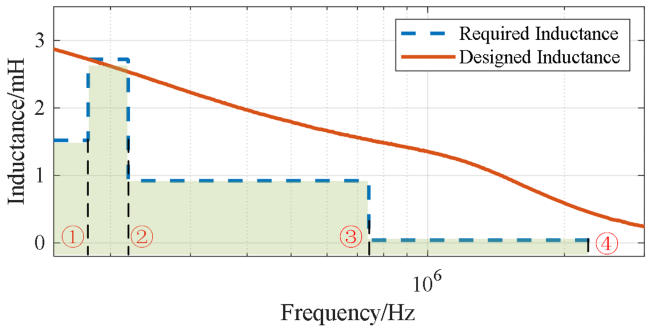

Fig. 29. Required and designed CM inductance.

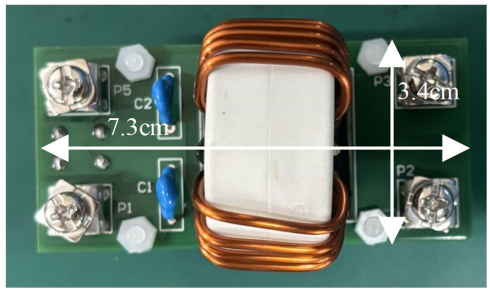

Fig. 30. Photograph of the designed CM Filter.

of the frequency-dependent inductance $L_{\rm cm}$ as shown in the blue dashed line in Fig. 29. The selected CM inductor should have a greater inductance than the threshold within the whole frequency range. A 3 mH prototype of a CM inductor is built based on nanocrystalline iron core, and its inductance is measured and also drawn in Fig. 29. It can be seen that the designed inductor can basically meet the requirement.

The designed EMI filter prototype is shown in Fig. 30, with a size of 73 mm×34 mm×25 mm, taking 9.2% of the size of the whole converter. The CM EMI of the whole system with the designed filter is tested and compared with the original EMI, as shown in Fig. 31. It can be seen that the EMI filter can well suppress the CM EMI below the standard line. The maximum peak of the CM EMI with filter appears around 220 kHz, corresponding to point ② in Fig. 29, where the designed inductance is a little bit below the required value. The required IL is then

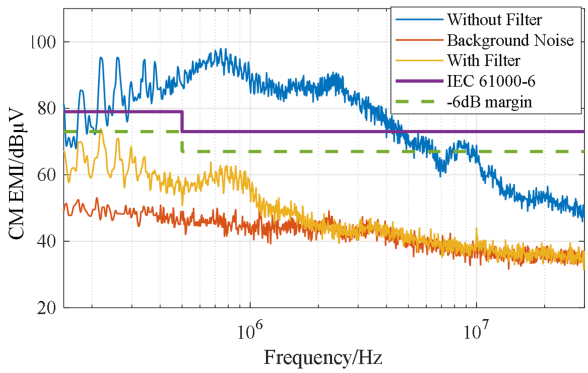

Fig. 31. CM EMI comparison with or without filter.

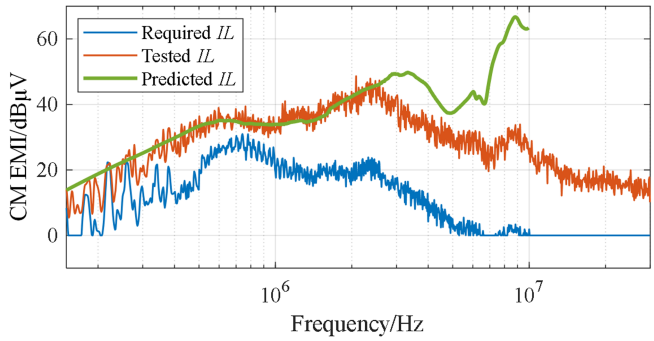

Fig. 32. Comparison between required, tested, and predicted IL.

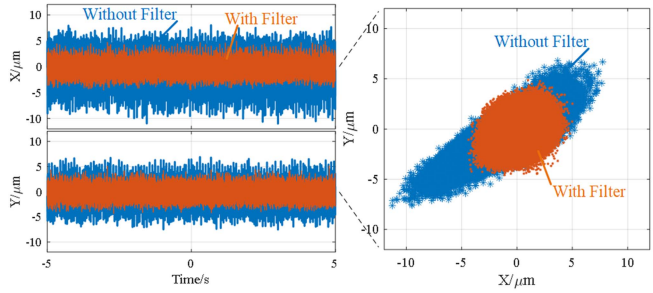

Fig. 33. Displacement comparison with or without filter.

compared with the tested and model-based predicted ones, as shown in Fig. 32. It can be seen that the predicted IL fits well with the actual measured one, which can further prove the accuracy of the CM model of the AMB system. Significant deviation appears in high-frequency range above 3 MHz, which is because the tested CM EMI is submerged by the background noise as can be observed in Fig. 31.

Furthermore, the displacement waveforms of the rotor under static floating are compared with or without the CM Filter, which is shown in Fig. 33. It can be seen that the designed filter can effectively reduce the interference on the displacement sensor, thereby enhancing the suspension accuracy.

VII. Conclusion

In this article, the HF CM model of the 5-DOF AMB system has been established, which can be further used to help design the EMI filters for AMBs.

We have found that the 5-DOF AMB system should be modeled as a 3-input 1-output system. Its impedance characteristics should be measured online because only then will there be an air gap between the stator and the frame. A V-I-based multiaxis online measurement scheme is proposed, with three independent measurements to identify impedance. It has been found that the signal processing method and the LCF between the three measurements would both affect the impedance extraction result. Therefore, the multispectral envelop algorithm is proposed to get better SNR, and the modified ZCMPWM is implemented to reduce the linear correlation coefficient in the entire frequency range. The lumped parameter equivalent circuits are established and two-step fitting with a genetic algorithm is proposed to extract the large number of parameters. The experiments have proved that the model built in this article can very well predict the CM EMI of the 5-DOF AMB system. Also, the IL of the CM EMI filter can be precisely predicted based on the proposed model, thus the filter can be well designed. The experiment results have proved that the implementation of CM EMI filter can significantly improve the levitation accuracy of the rotor.

References

[1] K. N. V. Prasad and G. Narayanan, "Electromagnetic bearings with power electronic control for high-speed rotating machines: Review, analysis, and design example," *IEEE Trans. Ind. Appl.*, vol. 57, no. 5, pp. 4946–4957, Sep./Oct. 2021.

[2] E. H. Maslen and G. Schweitzer, *Magnetic Bearings: Theory, Design, and Application to Rotating Machinery*. Berlin, Germany: Springer-Verlag, 2009.

[3] Y. Xie, D. Jiang, F. Hu, and Z. Liu, "Research on common mode EMI and its reduction for active magnetic bearings," *IEEE Trans. Power Electron.*, vol. 38, no. 4, pp. 4246–4250, Apr. 2023.

[4] B. Kagalwala and P. Shenoy, "Designing A hybrid variable frequency drive (VFD) with active magnetic bearing (AMB) for space applications," in *Proc. IEEE Int. Workshop Integr. Power Packag.*, 2022, pp. 1–6.

[5] A. D. Andrade, L. S. Haddad, R. Lateb, and J. D.Silva, "Comparative analysis of the performances and reliability of a switching power amplifier (SPA) for active magnetic bearing systems: SiC MOSFET vs Si IGBT version," in *Proc. Int. Symp. Magn. Bearings*, 2023, pp. 1–10.

[6] T. Hadden et al., "A review of shaft voltages and bearing currents in EV and HEV motors," in *Proc. IECON 42nd Annu. Conf. IEEE Ind. Electron. Soc.*, 2016, pp. 1578–1583.

[7] O. Magdun and A. Binder, "High-frequency induction machine modeling for common mode current and bearing voltage calculation," *IEEE Trans. Ind. Appl.*, vol. 50, no. 3, pp. 1780–1790, May/Jun. 2014.

[8] Y. Wu, H. Li, W. Ma, M. Dong, and Q. Zhong, "High-frequency model of permanent magnet synchronous motor for EMI prediction in adjustable speed drive system," in *Proc. IEEE Int. Power Electron. Appl. Conf. Expo.*, 2018, pp. 1–6.

[9] N. Idir, Y. Weens, M. Moreau, and J. J. Franchaud, "High-frequency behavior models of AC motors," *IEEE Trans. Magn.*, vol. 45, no. 1, pp. 133–138, Jan. 2009.

[10] L. Wang, C. Ngai-Man Ho, F. Canales, and J. Jatskevich, "High-frequency modeling of the long-cable-fed induction motor drive system using TLM approach for predicting overvoltage transients," *IEEE Trans. Power Electron.*, vol. 25, no. 10, pp. 2653–2664, Oct. 2010.

[11] Z. Zhao, F. Fan, W. Wang, Y. Liu, and K. Y. See, "Detection of stator interturn short-circuit faults in inverter-fed induction motors by online common-mode impedance monitoring," *IEEE Trans. Instrum. Meas.*, vol. 70, 2021, Art. no. 3513110.

[12] H. Jie, Z. Zhao, F. Fei, K. Y. See, R. Simanjorang, and F. Sasongko, "A survey of impedance measurement methods in power electronics," in *Proc. 2022 IEEE Int. Instrum. Meas. Technol. Conf.*, 2022, pp. 1–6.
[13] H. Chen and S. Ye, "Modeling of common-mode impedance of an inverter-fed induction motor from online measurement," *IEEE Trans. Electromagn. Compat.*, vol. 60, no. 5, pp. 1581–1589, Oct. 2018.
[14] X. Shang, D. Su, H. Xu, and Z. Peng, "A noise source impedance extraction method for operating SMPS using modified LISN and simplified calibration procedure," *IEEE Trans. Power Electron.*, vol. 32, no. 6, pp. 4132–4139, Jun. 2017.
[15] F. Fan, K. Y. See, X. Liu, K. Li, and A. K. Gupta, "Systematic common-mode filter design for inverter-driven motor system based on In-circuit impedance extraction," *IEEE Trans. Electromagn. Compat.*, vol. 62, no. 5, pp. 1711–1722, Oct. 2020.
[16] S. B. Rathnayaka, K. Y. See, and K. Li, "On-line impedance monitoring of transformer based on inductive coupling approach," *IEEE Trans. Dielectrics Elect. Insul.*, vol. 24, no. 2, pp. 1273–1279, Apr. 2017.
[17] H. Chen, S. Ye, T. Wang, X. Zheng, and T. Li, "Extraction of common-mode impedance of an induction motor by using all-phase FFT with intermediate-frequency filtering," *IEEE Trans. Electromagn. Compat.*, vol. 63, no. 5, pp. 1593–1598, Oct. 2021.
[18] D. Jiang et al., *Advanced Pulse-Width-Modulation: With Freedom to Optimize Power Electronics Converters*. New York, NY, USA: Springer-Verlag, 2021.
[19] M. Degano, P. Zanchetta, L. Empringham, E. Lavopa, and J. Clare, "HF induction motor modeling using automated experimental impedance measurement matching," *IEEE Trans. Ind. Electron.*, vol. 59, no. 10, pp. 3789–3796, Oct. 2012.
[20] J. H. Jun, B. I. Kwon, and B. T. Kim, "Analysis of bearing current of the inverter-fed induction motor using equivalent circuit parameters by FEM," in *Proc. 12th Biennial IEEE Conf. Electromagn. Field Computation*, 2006, pp. 142–142.
[21] C. Li, L. Zhang, T. Dong, T. Wang, and H. Chen, "An EMI receiver model with consideration of the intermediate frequency filter," in *Proc. 2016 Asia-Pac. Int. Symp. Electromagn. Compat.*, 2016, vol. 1, pp. 233–236.
[22] Z. Zhang, Y. Hu, X. Chen, G. W. Jewell, and H. Li, "A review on conductive common-mode EMI suppression methods in inverter fed motor drives," *IEEE Access*, vol. 9, pp. 18345–18360, 2021.
[23] H. Li, Y. Ding, C. Zhang, Z. Yang, Z. Yang, and B. Zhang, "A compact EMI filter design by reducing the common-mode inductance with chaotic PWM technique," *IEEE Trans. Power Electron.*, vol. 37, no. 1, pp. 473–484, Jan. 2022.

Yuanhao Xie (Graduate Student Member, IEEE) was born in Chongqing, China, in 1997. He received the B.S. degree in electrical engineering from the Chongqing University, Chongqing, China, in 2019. He is currently working toward the Ph.D. degree in electrical engineering with Huazhong University of Science and Technology, Wuhan, China.

His current research interests include power hardware-in-the-loop system, electromagnetic interference, and active magnetic bearings.

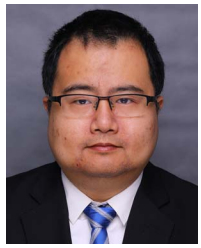

Dong Jiang (Senior Member, IEEE) received the B.S. and M.S. degrees in electrical engineering from the Tsinghua University, Beijing, China, in 2005 and 2007, respectively, and the Ph.D. degree in power electronics and motor drives from the University of Tennessee, Knoxville, TN, USA, in 2011.

He was with the United Technologies Research Center, East Hartford, CT, USA, as a Senior Research Scientist/Engineer, from January 2012 to July 2015. He has been with the Huazhong University of Science and Technology, Wuhan, China, as a Professor, since July 2015. His main research interests include power electronics and motor drives, with more than 200 published IEEE journal and conference papers and more than 70 granted patents in this area.

Dr. Jiang was the recipient of several best paper awards in IEEE conferences. He is an Associate Editor for IEEE TRANSACTIONS ON INDUSTRY APPLICATIONS.

Hui Liu (Graduate Student Member, IEEE) received the B.S. degree in electrical engineering from the Hefei University of Technology, Hefei, China, in 2021. He is currently working toward the Ph.D. degree in electrical engineering with the Huazhong University of Science and Technology, Wuhan, China.

His research interests include multilevel converters and electromagnetic interference of power electronics.

Zicheng Liu (Senior Member, IEEE) was born in Shandong, China, in 1989. He received the B.S. degree in hydropower engineering from the Huazhong University of Science and Technology, Wuhan, China, in 2011, and the Ph.D. degree in electrical engineering from the Tsinghua University, Beijing, China, in 2016.

During Otcober 2014 to March 2015, he was a Visiting Student with Purdue University, West Lafayette, IN, USA. During June 2016 to September 2018, he was a postdoc researcher with Beijing Jiaotong University, Beijing, China. He is currently an Associate Professor with HUST. His research interests include multiphase motor control systems and transportation electrification.